Title

Room temperature sensing of volatile organic compounds using hybrid SnO nanoflower and Laser-Induced Graphitic carbon devices

Authors

Richard Murray, Arbresha Muriqi, Cathal Larrigy, Alida Russo, Mintesinot Tamiru, Daniela Iacopino, Michael Nolan, Aidan J. Quinn*

*Corresponding Author: Aidan.Quinn@Tyndall.ie

Tyndall National Institute, University College Cork, Dyke Parade, Cork T12 R5CP, Ireland

Keywords

- Room Temperature Volatile Organic Compound Sensing
- Laser-Induced Graphene
- Additive Manufacture
- Resource Efficient Design
- Worker Safety
- Density Functional Theory

Highlights

- Room temperature volatile organic compound sensing
- Laser-induced graphitic carbon-nanomaterials hybrid devices
- Volatile organic compound sensor produced through an additive manufacturing process
- First demonstration of SnO-LIG chemiresistive sensor
- Validation of sensing mechanism by density functional theory calculations

Competing interest statement

The authors declare that they have no known competing financial interests or personal relationships that could have appeared to influence the work reported in this paper.

Graphical Abstract

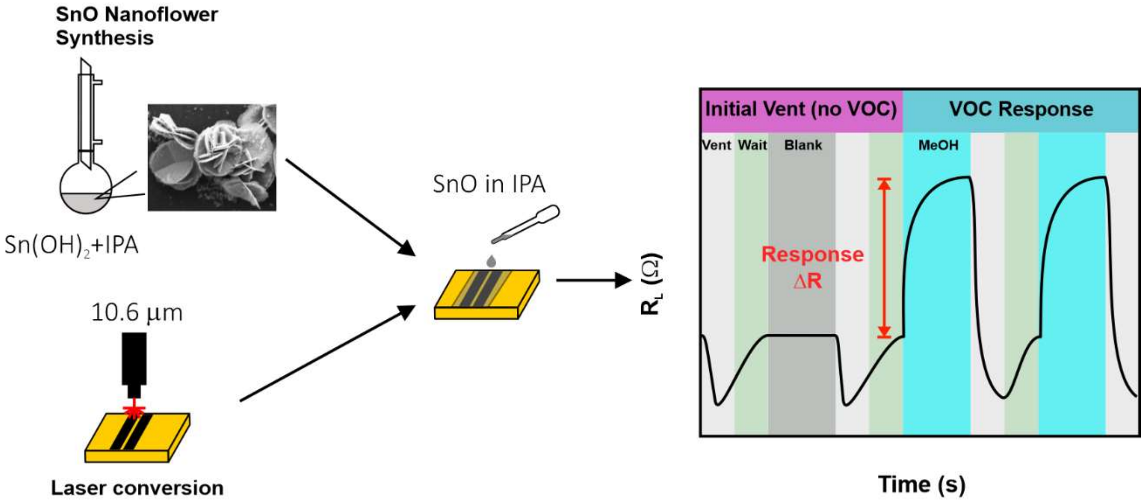

Abstract

Volatile organic compounds (VOCs) are a common risk to human health in industrial and domestic settings. VOCs are often present at concentrations that cannot be detected through human odor perception. VOC sensors are, therefore, urgently needed for home and workplace environmental monitoring, including wearable sensors for workers. However, current chemiresistive VOC sensors typically require high-energy fabrication processes with large environmental footprints, significant mass-loadings of critical raw materials and/or elevated operating temperatures, which hamper widespread, sustainable deployment. We demonstrate a simple, low-energy hybrid fabrication route for chemiresistive VOC sensors, comprising additively-produced laser-induced graphene (LIG) electrodes on plastic substrates, decorated with SnO nanoflowers. The SnO nanoflowers were synthesized below 100°C at ambient pressure and offer a low-energy alternative to conventional SnO_2 or other metal-oxide nanoparticle devices. These chemiresistive sensors can detect methanol vapor at room temperature (~18°C) and typical humidity levels (~55% RH), with a limit of detection (170±40 ppm) below 8-hour worker safety exposure levels (200 ppm). The sensors also demonstrated stable DC resistance responses $\Delta R/R = 9\pm2\%$ to 710 ppm of methanol for over 21 days in ambient laboratory conditions. First principles density functional theory simulations are used to elucidate the origin of the performance of the LIG-SnO sensors. LIG-SnO hybrid sensors thus present a resource-efficient route to develop chemiresistive sensors for low-power applications, such as wearable worker safety or Internet of Things edge-sensing.

Introduction

Many volatile organic compounds (VOCs) are released during industrial processes ranging from pharmaceutical manufacturing to automotive applications, as well as in domestic settings. They can originate as by-products of combustion, fuel storage, cooking, or through outgassing from household furnishings [1–7]. VOCs can also build up in enclosed spaces or areas with poor air exchange, resulting in increased local concentration and associated cumulative exposure risk [8,9]. Often, these VOCs pose a significant health risk at concentrations below human perception, e.g., methanol 8-hour worker safety threshold (200 ppm) vs. human odor detection (>10,000 ppm) [10–13]. Thus, reliable VOC sensors are necessary for worker and domestic safety through integration with the Internet of Things, either as worker wearables or as part of sensor networks within a workplace or domestic setting.

However, conventional VOC sensors typically use costly semiconductor-manufactured interdigitated metallic electrode platforms, requiring critical raw materials and increasing their environmental footprint [14]. Further, the sensitizing material typically requires high-temperature processing steps to produce the correct phase of the metal oxide (MOX) materials and/or to calcinate previously synthesized MOX nanoparticles [15,16]. Beyond that, they also often require elevated operating temperatures (>300°C), which pose significant challenges for low-power, wearable sensors. Therefore, there are three routes to reduce the lifetime energy cost of chemiresistive sensors: 1) the elimination of semiconductor fabricated electrodes, 2) lower energy preparation routes for sensitizing materials, and 3) room temperature operation.

Semiconducting MOX sensors were initially demonstrated as thin films, although recent advances using nanoparticle morphologies have led to decreased operating temperatures and mass loadings [17,18]. The MOX sensitivity to VOCs derives from the semiconductor conductivity dependence on charge carrier density. When a VOC adsorbs onto the MOX, a charge transfer produces a measurable conductivity change. The mechanism used to describe this is based on early thin film MOX VOC sensors, which described both the direct charge exchange process and a catalytically enhanced oxidation process occurring at elevated temperatures (>400°C) [18,19]. In the oxidation process, adsorbed/ionosorbed oxygen molecules withdraw electrons from the p/n-type MOX resulting in an increase/decrease of conductivity and producing different anions (O_2^-, O^-, O^{2-}) depending on the temperature. These high-energy charged species may react with VOC molecules and release the withdrawn electrons back into the MOX, undoing their previous modulation, upon exposure to a VOC molecule.

A great variety of MOX materials have been investigated for their sensitivity and selectivity to given VOCs, arising from adsorption site nature and adsorption energies dependences. These include n-type semiconducting MOXs, e.g., WO_3 [18], [20] ZnO [19], SnO_2 [20], TiO_2 [21], In_2O_3 [22][18]and also p-type: Co_3O_4 [23], CuO [24], Cr_2O_3 [25] and NiO [26]. To enhance their sensing performance (sensitivity, selectivity, stability, and response/recovery time), several methods have been developed, including: decoration with noble metal catalyst particles [15,27–29]; mixed-deposition of MOX nanoparticles [26,30–34]; morphology changes, including miniaturization [25,35–37]; high-aspect-ratio structures[38–40]; and use of hollow spheres [41–43].

These optimization routes, and combinations thereof, have been widely discussed in the literature [36,37,44–48]. Briefly, metal catalysts and MOX decoration can enhance reactant adsorption and allow spill-over [49] onto the MOX surface or can open additional reaction routes [50]. Morphological changes affect the sensor transduction behavior amplifying the charge accumulation or depletion layers and amplifying or attenuating device resistance, respectively, due to increased surface/volume ratios [37]. Similarly, p-n junction formation from MOX decoration can also contribute to surface depletion layer formation locally around the junction, producing a conduction route more strongly dependent on gas interaction [32].

However, such optimization routes typically require critical raw materials (e.g., Pt, Rh, Pd, Ti, W) [14], exotic fabrication conditions, and an increase of the complexity of the particle formation process without a significant reduction in device operating temperature. This yields sensor platforms that require significant resources for fabrication and operation, which need to be reduced further if they are to be used extensively as part of the Internet of Things. A comparison of typical sensor fabrication and operation conditions is presented in Table 1.

Table 1 Integration challenges for existing chemiresistive VOC sensing morphologies.

Sensor Type	Electrode	Support	Sensing Material Formation Temp. (>300°C)	Post calcination (>300°C)	Elevated Operational Temp. (>300°C)	Critical Raw Materials *	Ref
Thin Film	Pre-patterned Metal	Ceramic	Yes	No	Yes	Yes	[18,19,51–53]
Thick Film	Pre-patterned Metal	Quartz	Yes	Yes	Yes	Yes	[54–58]
Sintered Nanoparticles	Pre-patterned Metal	Ceramic	Yes	Yes	Yes	Yes	[15,27,59,60]
Self-assembled Nanoparticles	LIG Electrode	Polymer	No	No	No	No	This work

* Critical raw materials identified in Study on the EU's list of Critical Raw Materials (2020), e.g., Pt, Pd, Rh, In, Ti, W [14]

Semiconductor MOX nanoparticle investigations have typically favored n-type particles, in part due to their greater enhancement in sensing performance with particle size reduction than p-type MOX [24]. However, p-type materials have recently been demonstrated to have lower optimal operating temperatures than n-type MOX; this suggests their suitability for room temperature VOC sensors [61,62], which would dramatically reduce their energy consumption and allow for human wearable sensors. Further, p-type responsive sensors are invaluable for machine-learning-enabled e-nose sensor arrays, providing a discrete and opposite response polarity assisting in the fingerprinting of analytes [63].

Laser-induced graphitic carbon (LIG) is an attractive candidate electrode material for replacing traditionally manufactured electrodes. Discovered in 2014, this laser graphitization method enables site-specific direct-write formation of highly porous, three-dimensional, conductive carbon electrodes on suitable polymer substrates [64]. LIG was initially formed from polyimide, a synthetic polymer, using a 10.6 μm CO_2 laser. The laser treatment locally increases the temperature and pressure of the precursor polymer, producing the characteristic porous graphitic LIG material [65]. The complexity of the formation process necessitates multifactor optimization routines due to the multiple interrelated factors controlling morphology and behavior [66]. The resulting carbon material has shown great potential for electrochemical sensing [67,68], and energy storage [69,70] and more recently for gas sensing [71–74]**.** However, damaging/costly mechanical/silver-paint electrical contacts have been necessary to utilize the resulting carbon material, until recent direct-write, back-contacting methods were developed [70]. Subsequent works have demonstrated its formation from treated wood [75] and food products [76]; as-harvested renewables, e.g., cork [69]; and biopolymers, e.g., chitosan [77]. Further, its formation has been demonstrated using visible laser sources [78].

To date, LIG-based gas sensors have focused on NO_2 detection both as resource-efficient contact electrodes [71,72] and as active material [73,74]. These works have investigated LIG natively [74], and with MoS_2 functionalization [73], demonstrating impressive sensitivities and selectivities but with slow room temperature response/recovery times, ranging from several minutes to several hours. The response/recovery times become longer with the addition of humidity protection layers while further decreasing particle size results in faster response times, but slower recovery times, associated with strong binding to more numerous sites. These devices require the implementation of heating elements, either external or native Joule heating to decrease response/recovery times towards real-time monitoring applications.

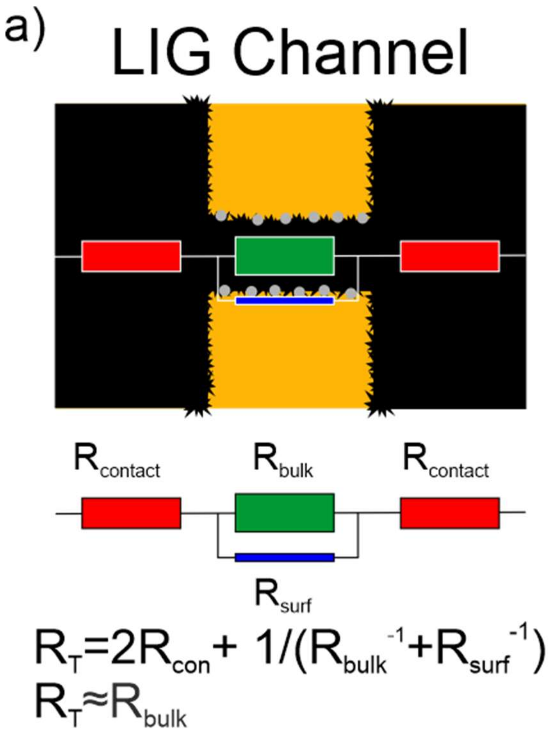

Figure 1 Schematic showing response sensitivity dependence on device functionalization geometry (channel vs. gap).

While LIG can be used as the sensing element, due to its formation condition tunable active sites, this sensor morphology should not be favored over interdigitated designs, where gas sensing is mediated by the sensitizing material in the gap region. Conduction through the LIG channel, even functionalized with sensitizing agents, acts as a parallel conduction path with the majority of the conduction mediated through the LIG bulk with a minor contribution from the surface/sensitizing layer, as shown in fig. 1a. Therefore, the effective modulation from gas species alters only the minor contribution of the surface resistance, but $R_{Total} \approx R_{Bulk}$. Even if large surface resistance modulation is achieved, it would still be a minority contribution to the measurable total resistance. In contrast, interdigitated geometries essentialize conduction through the sensitizing material in a series resistor network yielding a proportionally larger change in the measurable total resistance, as $R_T \approx R_{Gap}$, as shown in fig.1b.

Centering the device around the critical conduction channel results in enhanced responses, as has been demonstrated in the initial works using MoS_2 in both LIG channel (0.8 % response to 1 ppm of NO_2, 60°C) [74] and LIG gap-based devices (22.9% to 250 ppb of NO_2, room temperature) [71]. Further, LIG active material strongly cross-selects to humidity requiring the intervention of hydrophobic layers to mitigate its deleterious effects in channel-type devices [74]. Similarly, the high native selectivity of the LIG to NO_2 would be another undesirable cross-selectivity limiting functionalization towards other VOC analyte targets. Therefore, functionalized gap structures with LIG support electrodes, allow for electrode resource reduction and higher sensitivity, without introducing undesirable cross-selectivities.

These initial works on LIG-based sensors have focused on the use of MoS_2, however, molybdenum is a critical raw material [14]. This is not in line with the intent of using LIG as a resource-efficient sensing platform. Therefore, alternatives should be sought, one particularly attractive option is tin monoxide (SnO). SnO, like graphene and MoS_2 is a 2D layered material, due to the Sn 5s lone pair distorting its crystal structure [79,80] allowing for enhanced surface/volume ratios and accessible 5s orbitals [81]. This, in addition to its p-type semiconducting nature due to Sn vacancies [80,82,83], and its metastability up to moderate temperatures (370°C), make it an attractive candidate for room temperature VOC sensing [84]. However, to date there have been limited investigations using SnO, preferring instead SnO_2 due to its well-established synthesis route, despite its high-temperature preparation and calcination process steps (400-800°C) [85]. Further SnO presents a viable route for sensitivity enhancement via p-n junction surface depletion layers through controlled oxidation of SnO (p-type) into SnO_2 (n-type).

While SnO_2 has received more research interest due to its early adoption as the preeminent gas sensor since the 1970s [20,54] there have been some more recent works exploring SnO as a gas-sensing material [62,86,87] and for Li-battery applications [88–90]. SnO has been prepared in several ways including evaporation/sputtering [38,84,91], carbothermal [92], hydrothermal [93–95], sonothermal [96,97], microwave [98] and solution methods [87,89]. However, evaporative/sputtering routes due to their high-energy preparation tend to yield p-type SnO thin films with uncontrolled n-SnO_2 surface contaminations [62,86,99,100]. Oxygen-poor environments such as carbothermal preparations or nitrogen-protected synthesis environments yield n-type SnO due to oxygen vacancies [81,87]. In solution routes interesting and complex morphologies (frames, bowls, pompon, etc.) of SnO, suitable for VOC detection, have been demonstrated in amine-based and long-chain organic solvents under solvothermal synthesis routes [87,101]. If SnO is to be adopted as a MOX VOC sensor, its preparation will require controllability, scalability, and green synthesis chemistry. Simple and easily scaled reflux chemistry routes using green solvents to produce SnO particles suitable for VOC detection with reduced energy cost are available with reflux-solvent-controlled particle morphology [89]. This work combines IPA reflux synthesis prepared p-type MOX SnO nanoflowers and additively manufactured conductive LIG to produce novel VOC sensors. This system requires only a low mass-loading of the SnO nanoflowers to achieve VOC sensitivity at room temperature. The resulting device requires fewer resources to produce and operate and is both sensitive and stable at ambient humidity and room temperature, all essential for application as resource-efficient VOC sensors for future applications, including worker safety.

Experimental Section

Device Fabrication

Laser Graphitization

Adhesive-backed polyimide tape (Radionics, 70 μm, HB830) was drawn and affixed to clean glass slides, ensuring no air bubbles were trapped. The polyimide top surface was converted to laser-induced graphene by CO_2 laser (10.6 μm, 30 W, Universal Laser system, PLS4.75) raster patterning at 4.2 W average laser power, ~200 mm s^{-1} scan speed (1000 pixels per inch, PPI) and ~20 lines mm^{-1} raster line density. Smooth edges were defined by a vector write (3.7 W average laser power, ~200 mm s^{-1} scan speed and 1000 PPI), yielding two parallel rectangular carbon electrodes (10 mm X 3 mm) separated by ~100 μm.

Particle Synthesis

SnO nanoflowers were synthesized following the method of *Jaśkaniec et al.*[89]. Anhydrous $SnCl_2$ (7.56g, Merck, 98%), was dissolved in deionized (DI) water (18.2 MΩ cm, 400 mL) in an ice bath. Ammonium Hydroxide (NH_4OH, 10 mL, 28%, Merck) was added dropwise while stirring, yielding a white precipitate, which was centrifuged and then washed with DI water and isopropyl alcohol (IPA, Merck, 99.7%). 3 g of this precipitate was dispersed in 60 mL IPA and refluxed while stirring in a mineral oil bath at 90°C for 18 hours until a brown/black dispersion was produced, which contained the SnO nanoflowers.

Device Fabrication

250 μL of the *as-produced* SnO nanoflower dispersion was added to 2 mL of IPA. 25 μL of the dilution was then dropcast onto the *as-fabricated* LIG electrodes and allowed to dry overnight yielding the VOC sensors. These devices were electrically contacted with mechanical clips.

Material Characterization

Raman

Raman spectra were acquired at multiple regions across the functionalized Laser-Induced Graphitic Carbon-SnO hybrid sensor (Horiba XploRA Raman microscope, 532 nm, 50× objective, 2,400 sample grating, 60 s sampling time, 1 accumulation, 1% filter). Spectra are reported without background subtraction or smoothing.

XRD

Precipitated nanoflowers were dried and deposited onto double-sided tape on microscope slides to produce a powder film. A θ–2θ powder X-ray diffraction scan (PANalytical X'pert PRO XRD, copper anode, $K_{\alpha 1}=1.5406$ Å, $K_{\alpha 2}=1.5444$ Å, ½° divergence slit, generator voltage 45 kV, 40 mA), was acquired between 20° and 80°.

Microscopy

Scanning electron microscopy (SEM) images of LIG-SnO nanoflowers, covered with ~6 nm of Au, to reduce charging effects, were acquired using an FEI Quanta 650 scanning electron microscope (10 kV beam voltage).

Gas Sensing

We developed a simple system for headspace VOC vapor detection from multiple SnO-LIG sensors under controlled humidity conditions. This resource-efficient system would be within the budget of many undergraduate teaching labs.

Experimental setup for headspace vapor detection

An Arduino-controlled solenoid valve was employed to allow time-controlled venting of a dry nitrogen line, while maintaining consistent pressure (Supporting Information Fig A.3.1). The dry nitrogen line was divided into two paths, each connected to a flow controller. One line was connected to a bubbler containing deionized water, with check valves to prevent backflow, and then to a condenser. The humidified condenser output line and the dry nitrogen line rejoin in a mixer. The relative humidity of the nitrogen line was controlled by changing the ratio of the gas flows at the flow controllers to match ambient room humidity (~55-65% RH) as verified by a humidity detector (RS-192TK Temperature and Humidity Datalogger).

Gas Sensing

The functionalized sensors were mounted in a 3D-printed sample holder, S.I. Fig. A.1.1, and electrically contacted with a maximum of 6 sensors per chamber. A 100 MΩ balancing resistor was connected in parallel to each device, Fig. A.2.1, to reduce the equivalent circuit resistance below the limit of the multi-channel multimeter used (Keithley DAQ 6510, 7700-20 slot card). Devices were measured simultaneously via multiplexing (NPLC (number of power line cycles) = 5, time between measurements: 100 ms) at laboratory room temperature (~18°C).

Cycles of separately humidified nitrogen gas vents and liquid phase solvent additions (1 μL-100 μL were carried out using micro-syringes (Hamilton, 10 μL/50 μL/100 μL) while monitoring the device resistance to determine the solvent response. The vapor phase concentration (ppm) arising from liquid phase aliquots of target individual VOCs (methanol (99.8%, Merck), ethanol 99.9%, Ocon), isopropyl alcohol (99.5% Merck), acetone (99.5%, Merck)) was verified using a photoionization detector (Tiger PID, 11.7 eV lamp), standardized against a reference gas (100 ppm isobutylene in balance air).

Aging study

6 sensors were mounted in the sample holder and electrically contacted. Their sensing responses to 1 μL of methanol (~150 ppm) and 5 μL (~710 ppm) were recorded on the initial and subsequent days. The laboratory temperature and humidity were recorded each day and the vent humidity was set to match the laboratory humidity (~ 55-65% RH).

Computational Methods

Density functional theory (DFT) calculations were employed to investigate the interaction of MeOH, EtOH, IPA, Ace and water at two specific low-energy facets of SnO: (001) and (101) [89,102]. Calculations were conducted using a periodic plane wave basis set implemented in the Vienna Ab initio Simulation Package (VASP) version 5.4 [103]. Core electrons were treated through the projector augmented wave (PAW) method and the valence electronic configurations used are: Sn: $5s^2 5p^2$, O: $2s^2 2p^4$, C: $2s^2 2p^2$, and H: $1s^1$ [104]. We employed the Perdew–Burke–Ernzerhof (PBE) approximation to the exchange–correlation functional [105]. The plane wave cut-off is 400 eV, and a Monkhorst−Pack sampling k-point grid of (3 × 3 × 1) is used for both surfaces. The force convergence criteria was set at 2×10^{-2} eV Å^{-1}, while the energy convergence criteria is 1×10^{-4} eV. The equilibrium lattice parameters of SnO from this set-up are $a = b = 7.59$ Å, $c = 24.03$ Å, and $\alpha = \beta = \gamma = 90°$ for the (001) SnO surface and $a = 12.39$ Å, $b = 7.62$ Å, $c = 23.93$ Å, and $\alpha = \beta = \gamma = 90°$ for the (101) SnO surface.

Adsorption energies were calculated using the following equation:

$$E = \sum E_{product} - \sum E_{reactant}$$

Where $\sum E_{product}$ is the summed energy of the product species and $\sum E_{reactant}$ is the summed energy of the reactant species.

Results and Discussion

Laser-induced Graphitic carbon (LIG) has been reported by *Tour et al.* as a thermal conductivity-based VOC sensor [106], and by *Paterakis et al.* as a capacitive humidity sensing platform [107], due to its high specific surface area, low resource cost, and ease of fabrication. Recently, LIG has been demonstrated as a chemiresistive sensing element for the detection of NO_x [71–74]. However, these works typically used critical raw materials (MoS_2) for functionalization. This work, demonstrates for the first time the combination of LIG as a low-resource cost current collector for a chemiresistive volatile organic compound (VOC) sensing platform, which is functionalized with a low mass loading of earth-abundant semiconducting metal oxide (MOX) nanoparticles, namely tin monoxide (SnO). This platform delivers the benefits of the LIG current collector with an inexpensive, widely available metal oxide sensing platform, overcoming issues associated with high-cost semiconductor fabricated VOC sensors.

This work used LIG as an electrode platform functionalized with separately synthesized p-type SnO nanoflowers to produce a VOC sensor. The sensors required only a low mass loading of SnO nanoflowers and two LIG electrodes separated by a small gap (~100 μm). A low-cost, homemade, 3D-printed sensing chamber lid and conventional lab glassware were used to mimic VOC headspace detection under ambient conditions.

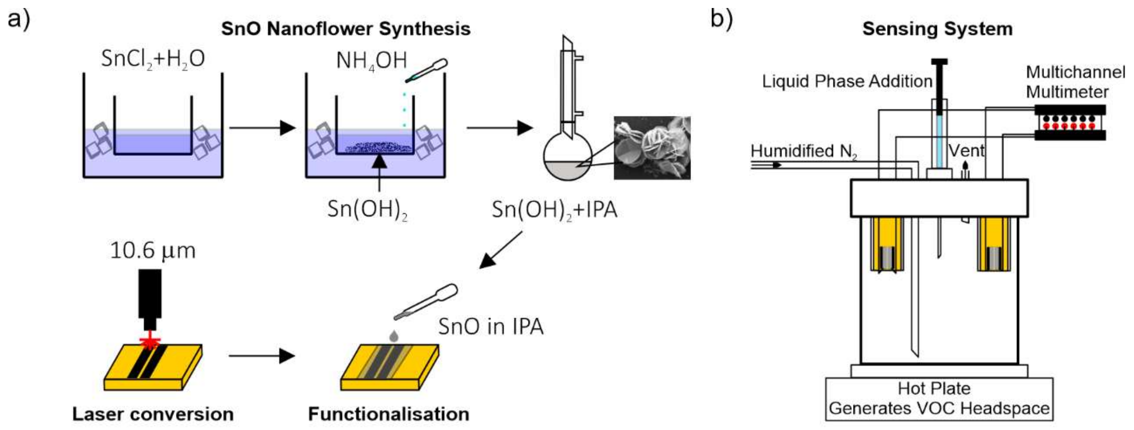

Figure 2 a) Summary process flow for SnO synthesis, Laser-Induced Graphitic carbon formation and drop casting to produce VOC sensors, b) Schematic of VOC sensing apparatus.

Fig. 2a schematically shows the synthesis of SnO nanoflowers, following the method of *Jaśkaniec et al.* with an IPA reflux solvent, and its combination with separately prepared LIG electrode (gap width ≈100 μm) to produce a VOC sensor [89]. Six dried sensors were mounted in a custom, 3D-printed sample holder (see A.1) and electrically contacted, and placed into a 600 mL glass flask, see Fig. 2b. A Hotplate, 80°C, beneath the sensing chamber ensures rapid evaporation of the injected solvent to produce VOC headspace vapor. Sequential liquid phase additions (Hamilton μL syringe 10 μL, 50 μL, 250 μL) of analyte VOCs and humidified N_2 vents (matched to ambient humidity ~55-65% RH, see A.3), were carried out to investigate the VOC sensitivity induced by the SnO nanoflowers. The baseline resistance of the sensors (~GΩ) exceeded the maximum measurable resistance of the multimeter used (Keithly DAQ 6510), vs. its 100 MΩ detection limit. Therefore parallel balancing resistors (100 MΩ) were used to reduce the overall circuit resistance below the equipment measurement limit (see A.2).

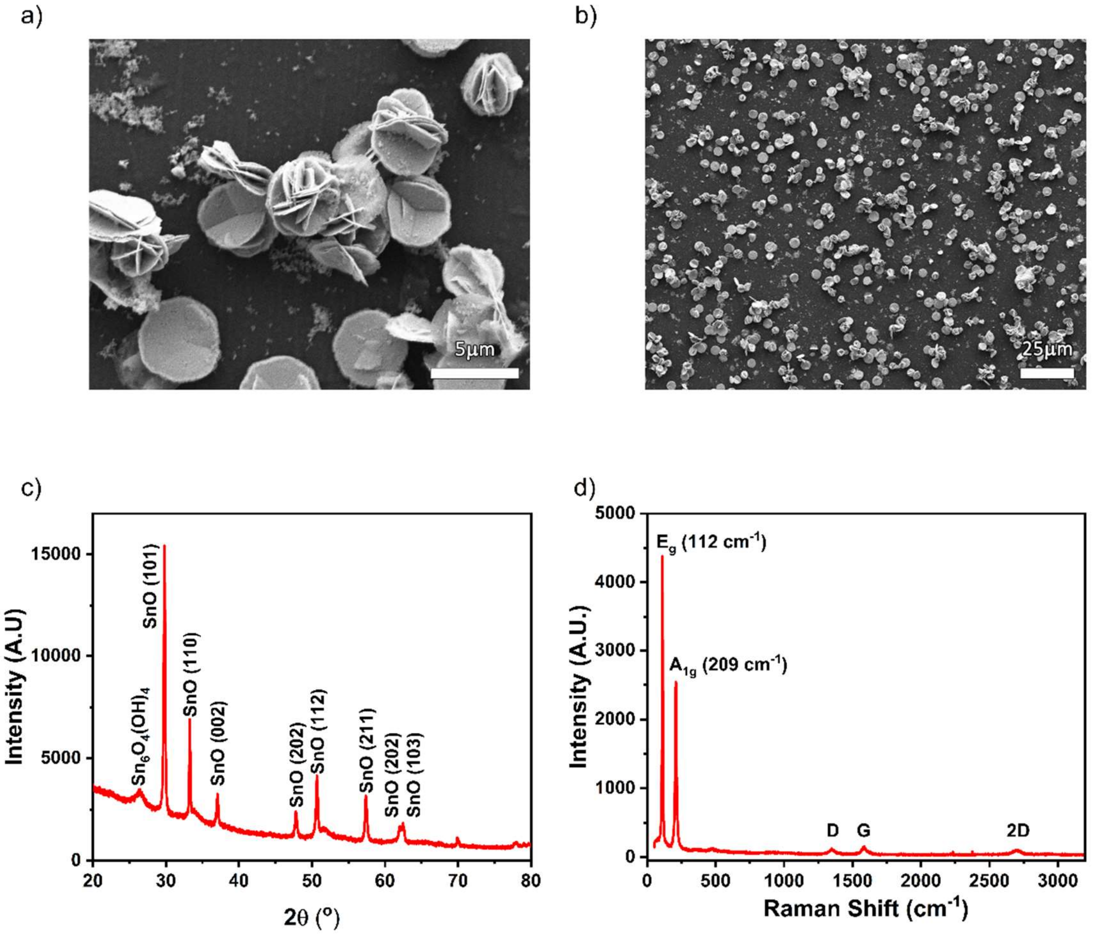

Figure 3 a) Scanning electron micrograph demonstrating the SnO nanoflower flower-like morphology. b) Scanning electron micrograph of SnO nanoflowers drop cast on polyimide film displaying disordered, random aggregation. c) Powder X-ray diffractogram of as synthesised SnO nanoflowers on a supporting glass slide. d) Raman spectrum of SnO NP on LIG electrode surface.

Figure 3 shows the microstructure, crystal phase and oxidation state of the synthesized SnO nanoflowers. Fig. 3a demonstrates the expected interlocked disc nanoflower structure for particles produced in IPA [89]. The flower morphology comprises intersecting micron-scale disks with diameters of 4.0 ± 0.5 µm and thickness ≈ 400 nm (see Fig. B1). SnO forms through a dissolution-reprecipitation process of intermediated $Sn_6O_4OH_4$ to produce nanoscale plates that aggregate into larger structures [85,94]. A_{1g}/E_g peak area ratios correspond inversely with number of layers of SnO [108]. We found A_{1g}/E_g peak area ratios ranging from 1.35-1.94, which correspond to bulk layers down to approximately

10-layers, which matches well with the large nanoflower particle structures. Assuming a Lorentzian Peak shape and applying the Scherrer formula for the (101) peak we find crystallite size of ≈ 1.08 nm in the direction perpendicular to the plane. This deviates from the observed particle thickness which is on the order of 100 nm and corresponds with a mesoscale structure composed of numerous aligned nanoparticle building blocks as observed for SnO in the literature [94].

When dropcast and dried on untreated polyimide, the IPA-suspended nanoflowers form a sparse, discontinuous, self-aggregating network (Fig. 3b). Fig. 3c shows the X-ray diffractogram of the as-synthesized nanoflowers, characteristic of the expected romarchite phase of SnO (JCPDS 06–0395 space group P4/nmm), with an additional broad peak, ascribed to unconsumed $Sn_6(OH)_4O_4$ [89,109]. The SnO oxidation state is further verified through Raman spectroscopy (Fig. 3d), which shows the characteristic B_{1g} and A_{1g} peaks at 112 cm^{-1} and 209 cm^{-1}, respectively, without any peaks that would correspond with SnO_2 formation [109]. This confirms the successful synthesis of the high-surface-area, MOX SnO nanoflowers, although with some unconverted $Sn_6(OH)_4O_4$. The nanostructured surface enhances the surface area-volume ratio, increasing the adsorption sites, while the p-type semiconductor nature of SnO, verified by a Mott-Schottky plot (Fig. C.1), should result in decreased conductivity upon electron transfer [110–112]. Given that many VOCs are reducing gases (electron-donating), the resistance through the particle network should therefore increase upon VOC exposure.

In the absence of residue from LIG formation, the random aggregation of nanoflowers on polyimide does not produce effective conduction channels, unless a high-mass-loading dense film is used. Instead, LIG provides a scaffold for the aggregation of particles in the interelectrode gap region. LIG is produced by raster scanning of a CO_2 laser source over a precursor substrate. This process has been optimized to produce high-quality graphitic material, with low sheet resistance, high surface area, and controlled surface morphology and dimensions [66]. Redeposition of graphic material and lateral growth of LIG occurs as a side-effect of the laser graphitization process. While these effects may limit the ultimate lateral critical dimensions of LIG devices, they also offer a route to promote local aggregation of SnO nanoflowers and enable the formation of hybrid LIG-nanoflower conducting networks with minimal SnO nanoflower mass loading, while maintaining a gap-like sensor geometry.

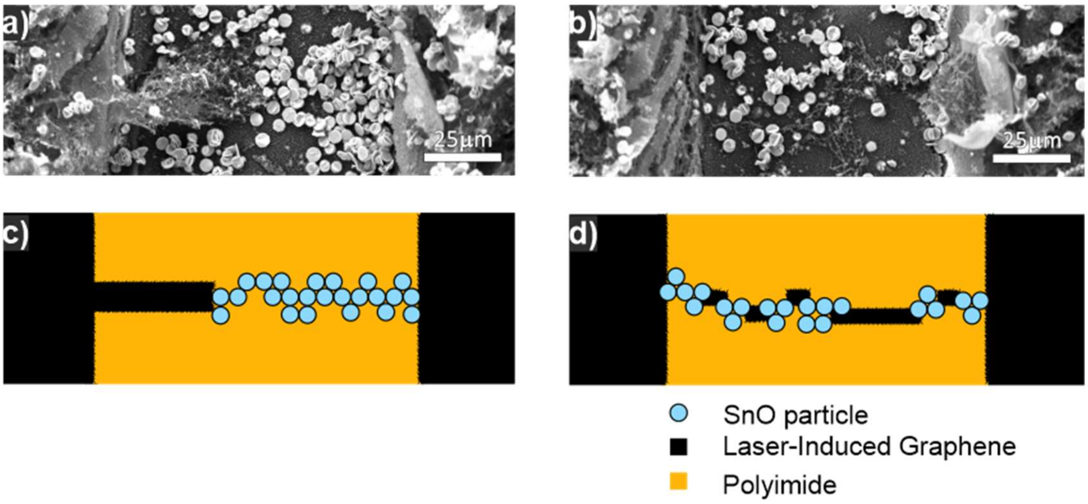

Figure 4 a) Scanning electron micrograph of partial hybrid carbon bridge-SnO nanoflower mediated conduction channel. b) Scanning electron micrograph of hybrid carbon islands-SnO nanoflower mediated conduction channel. c) Schematic of carbon bridge-SnO mediated conduction channel. d) Schematic of carbon islands-SnO mediated conduction channel.

Figure 4 shows examples of hybrid-SnO-LIG electrode bridging conformations in device gap regions. The carbon inclusions act both as a scaffold for the nucleation of SnO particles during the evaporation of the drop-casting solvent and to reduce the effective gap width. Devices consist of multiple, separate quasi-parallel LIG-SnO conduction channels (1+1 D network). The dominant conduction pathways can be viewed as either a LIG "bridge" (Fig. 4a,c), which connects the contact electrode to a nanoflower aggregate, or LIG "stepping-stones" (Fig. 4b,d), which connect multiple separated nanoflower aggregates. Other pathways and failure modes are demonstrated and discussed in Appendix D.

Conduction across the interelectrode gap, therefore, includes contributions from the semiconducting nanoflowers (intrinsic p-type SnO), which dominate the device resistance, and the conductive LIG graphitic material. Given the room temperature operation of the sensors presented in this work, conventional ionosorbed oxygen models used to describe high-temperature semiconductor MOX sensors with full reduction of analytes are not appropriate [48,54,55,113]. However, the effect of MeOH molecular adsorption onto p-type nanoflowers could be considered in terms of electron density transfer to the MOX surface, either directly or else indirectly; mediated by adsorbed oxygen species. This could reduce the net hole carrier density at the nanoflower surface, leading to increased device resistance for aggregated nanoflower networks. Further, we note that no appreciable variation in sensing performance was observed, when operating in dry N_2 or dry air environments, suggesting no significant dependence on atmospheric oxygen. Control LIG devices fabricated without SnO nanoflowers showed no appreciable change in device resistance upon exposure to VOC vapors.

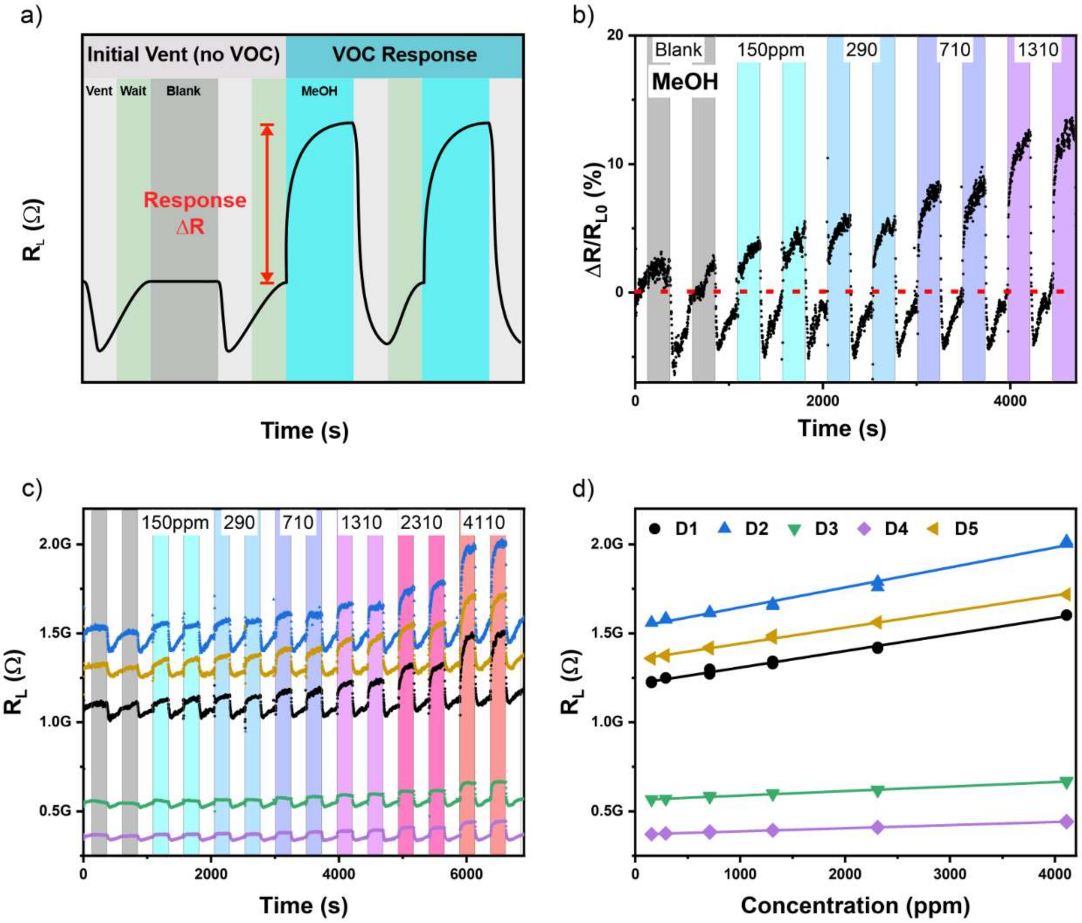

Figure 5 a) Schematic of sensing response behavior to methanol exposure. b) Response curve for a single representative VOC sensor, colored bars highlight the addition of methanol. c) Grouped response curves for five sensors monitored simultaneously during a sequentially higher methanol concentration exposure. d) Calibration curve of simultaneously monitored sensors responding to MeOH solvent additions, demonstrating a mean Limit of Detection <200 ppm.

Figure 5a schematically depicts the DC resistance response of one of the hybrid SnO-LIG VOC sensors in the custom chamber, which was designed to mimic headspace detection of VOC vapors at ambient temperature (~18°C). Each run begins with one or more “blank” cycles to measure baseline behavior without introducing the VOC solvent. For each blank cycle, the sensing chamber (≈0.6 L volume) is purged with humidified nitrogen for 2 minutes (> 20 L/min., ~55-65% RH, matched to lab. humidity). The system is allowed to equilibrate for 2 minutes, followed by a 4-minute “blank” period. Following another “vent/wait” purge cycle, an aliquot of the VOC solvent is added using a micro-syringe and evaporates after landing on the heated chamber base. The response value, ΔR_L, is taken as the resistance increase ≈ 3 mins after VOC addition, corresponding with the steady-state measurement of gas phase VOC concentration using a photoionization detector, see Fig. E.1. Figure 5b shows a typical sensor response normalized to the initial resistance ($\Delta R_L/R_{L0}$) during multiple cycles over a low MeOH concentration range from 150 ppm (1 μL aliquot) to 1310 ppm (10 μL aliquot). The data show clear response increases with increasing VOC concentration.

Figure 5c demonstrates the reproducibility of 5 sensors simultaneously exposed to the same concentration ramp (one device was excluded due to instability, shown in Fig. D.4). The response shape and percentage responses of these devices are similar, despite their varying baseline resistances. A slight increase in the baseline is observed at higher concentrations (≥2310 ppm). This is characteristic of incomplete venting. However, since the saturation concentration of the MeOH headspace was measured under identical conditions (Fig E.1), the measured response accounts for this cumulative build-up at larger aliquot volumes. The MeOH response/concentration curves for these sensors are presented in Fig. 5d, with corresponding limits of detection (LOD) tabulated in Table 2. The mean LOD for methanol, 170±40 ppm; is below the 8-hour OSHA and EPA worker safety limit of 200 ppm [10–12].

Table 2 Limit of detection of methanol and ethanol extracted from Fig. 4d and 7b respectively.

Solvent	**Device 1 LOD (ppm)**	**Device 2 LOD (ppm)**	**Device 3 LOD (ppm)**	**Device 4 LOD (ppm)**	**Device 5 LOD (ppm)**	**Mean LOD (ppm)**
Methanol	149±3	225±8	167±4	197±6	122±2	170±40
Ethanol	210±9	188±8	106±2	205±9	179±7	180±40

The device-to-device variability in baseline resistance data (Fig. 5c) reflects the proposed conduction mechanism through self-aggregated SnO nanoflowers partially bridged by LIG. As noted above, the sensors show consistent response magnitude, shape and time dependence. For some devices with a high degree of carbon bridging (lower initial resistance), the sensor becomes less sensitive at high methanol concentrations (Fig. D.3) suggesting that the degree of carbon bridging could provide a viable route for future optimization.

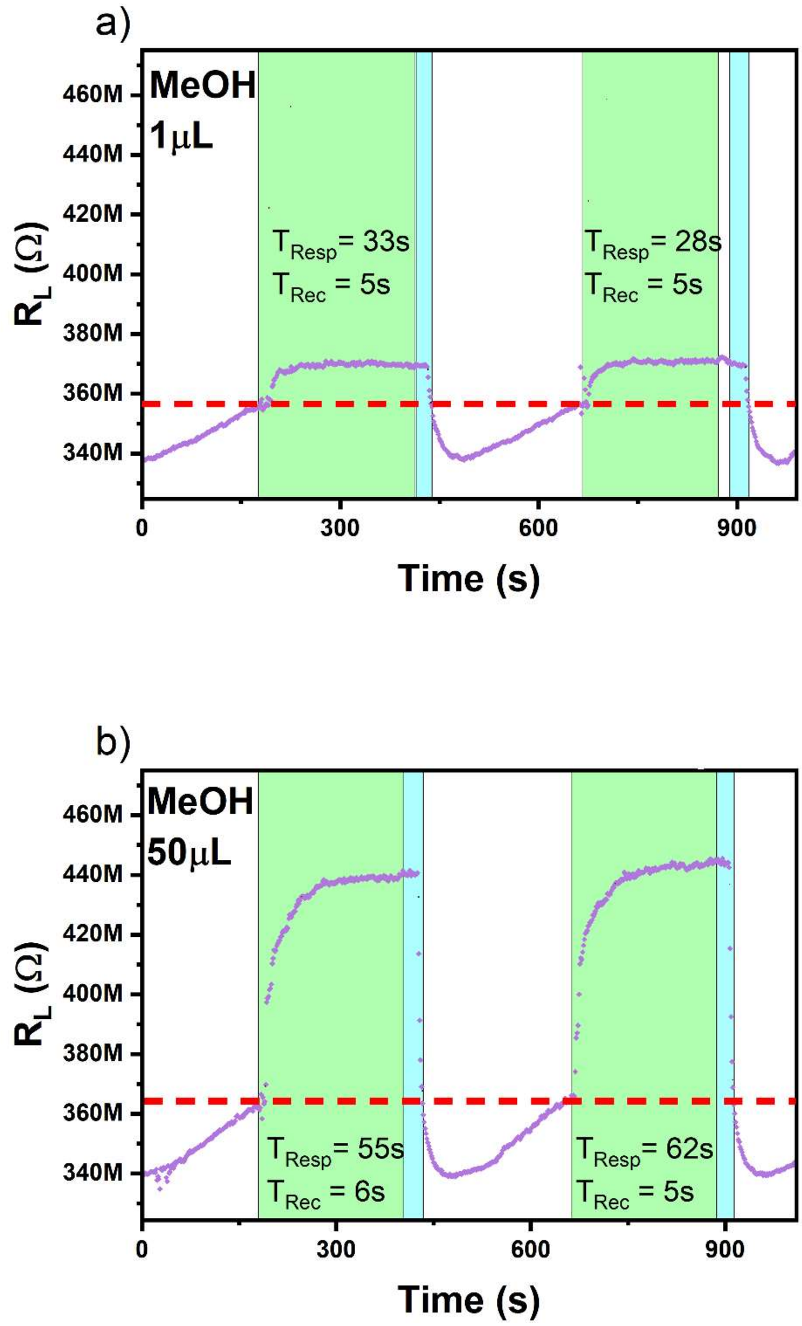

Figure 6 a) Sensor response and recovery time towards 1 μL (150 ppm at saturation) of MeOH. b) Sensor response and recovery time towards 50μL (4110 ppm at saturation) of MeOH.

The methanol addition response time is presented in Fig. 6. The time taken to rise to 90% of the maximum response (t_{90}) was $t_{90} \approx 30$ s for 1 μL (150 ppm) of methanol and $t_{90} \approx 57$ s for 50 μL (4110 ppm) of methanol. It is likely that the simple liquid phase addition-evaporation method employed here to generate headspace VOCs aliases the measured response time with the evaporation rate. For example, for the same chamber base temperature, we observe greater response times for ethanol (t_{90}

≈ 45 s for 1 μL), which has a higher boiling point than methanol. Therefore, we consider the measured response times to be an upper bound. The recovery time, ≈ 5 s, was unaffected by increased VOC concentration levels. We note that the solvent introduction method employed here enables resource-efficient study of a variety of VOC compounds and serves as a versatile pathfinding route to assess new sensor configurations.

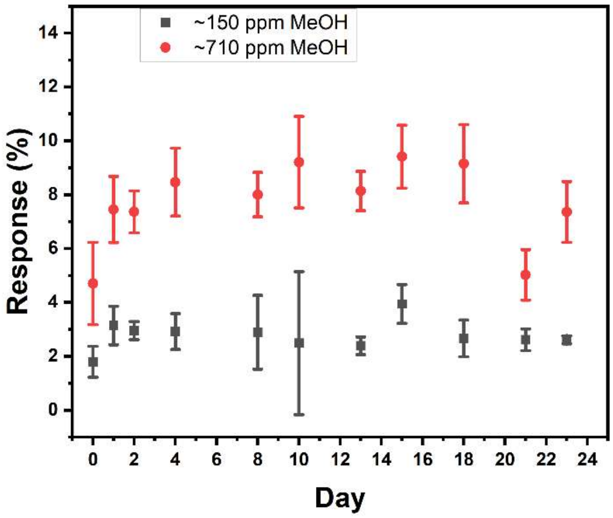

Figure 7 Mean (n=4) response stability behavior of SnO-LIG hybrid sensor towards 1 μL (150 ppm) and 5μL (710 ppm) of MeOH with aging.

Figure 7 shows the stability behavior of a set of four SnO-LIG hybrid VOC sensors monitoring MeOH detection across 21 days. No degradation of sensing behavior is observed associated with the age of the sensor or due to the cumulative exposure to MeOH over in the time window studied. The sensors demonstrated DC resistance responses ΔR/R = 9 ± 2% to 5 μL aliquots of methanol (~710 ppm) for over 21 days in ambient conditions, without signs of ageing. The device variability reflects changes in laboratory temperature and humidity over the period (Fig. F.1). Reduced variability was observed for moderate laboratory temperatures (16-20°C) vs lower temperatures (13-16°C), see Fig. F.1d.

Figure 8a shows the cross-selectivity behavior to ethanol, IPA and acetone. We observe comparable response ($\Delta R_L/R_{L0}$) values for methanol (8.3±1.0%), ethanol (12.5±1.9%), and acetone

(8.8±0.7%). The response data for IPA demonstrates incomplete recovery behavior, suggesting a high adsorption affinity at the SnO nanoflowers. This is not unexpected, given that IPA was the reflux solvent for their synthesis. Figure 8b shows the response data vs. time for an ethanol concentration ramp for our LIG-nanoflower devices and Fig. 8d shows the corresponding concentration-response curves. The mean extracted LOD for ethanol is 180±40 ppm (Table 2), similar to the mean LOD for methanol, 170±40 ppm.

The mechanism for VOC detection on SnO at room temperature is challenging to establish experimentally and is therefore not described in detail in the available literature. Chemiresistive MOX sensors are typically considered in terms of an oxygen-mediated process, devised in 1962 by *Seiyama et al*. [19]. This route typically assumes a high temperature of operation to achieve oxygen radicals, or charged oxygen species at more moderate temperatures. This mechanism has received broad adoption due to its prevalence at high temperature and for noble metal decorated MOX systems, catalyzing oxygen ionisation [49,55,113]. However, it may not be generalizable to room temperature processes. Alternative mechanisms have been proposed, including water-mediated routes, and direct adsorption with charge exchange. Water-mediated routes have been demonstrated at room temperature on Fe_2O_3, depending on the formation of hydroxyl groups mediating the charge exchange [114]. Similarly, direct adsorption and charge exchange have also been proposed to explain the electron withdrawal of NO_x on MoS_2 at room temperature [72].

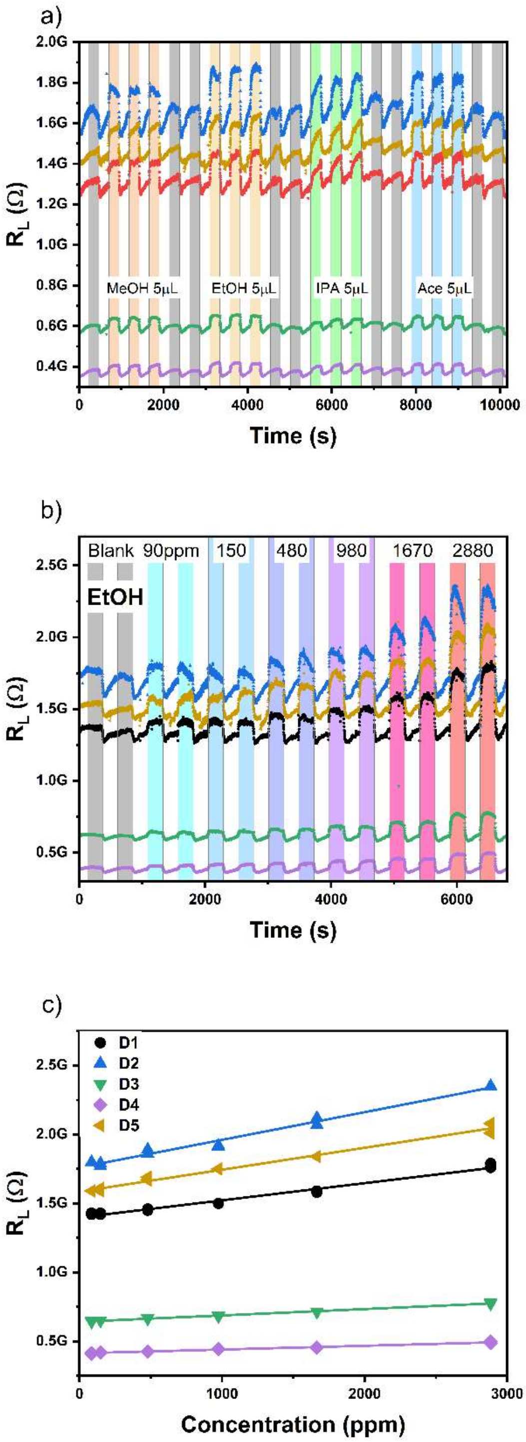

Figure 8 a) Cross-selectivity response towards 5 μL of MeOH, EtOH, IPA and Acetone. b) Response curve for five VOC sensors simultaneously exposed to the same ethanol concentration ramp, colored bars highlight the addition of ethanol. c). Calibration curve of simultaneously monitored sensors responding to EtOH solvent additions, demonstrating a mean Limit of Detection <200 ppm.

The response of SnO to various reducing gases in this work was conducted using a humidified nitrogen gas flow. The sensing mechanism is unlikely to be oxygen mediated, as the nitrogen gas flow would provide no oxygen to restore those consumed on the MOX surface, and no significant drift between measurements was observed. Similarly, no significant dependence on humidity was observed. Consequently, the interaction between analyte gases (methanol, ethanol, isopropanol, acetone, and water) and SnO surfaces is expected to be an adsorption/charge exchange-based process.

The SnO nanoflowers are composed of two main planes; the flat regions (001) planes and the edges (101) planes [89]. These particles aggregate at carbon debris forming a self-assembling SnO nanoflower network between the current collectors, as shown in the SEM micrographs, fig. 4. Due to their layered aggregate nanoflower structure, the granular network of SnO particles deviates from the typical homogenous surfaces of spherical/rod/wire structures implicitly assumed in MOX chemiresistive sensors. Instead, there are numerous particle junctions. Due to the flower morphology, the particles will interface at (101) planes, rather than (001) planes as the petals block the overlap of (001) planes. Therefore the conduction path is comprised of a series of (101) interfaces and parallel paths through (001) top surfacs and (001) bulk regions. Consequently, the selectivity and degree of interaction of a given analyte will depend on the morphology of the particles used and the relative contributions of these two planes.

The conductivity through the (001) direction depends on a combination of the thickness of the (001) bulk and the degree of surface depletion layer thickness. In large particles, conduction is dominated by the bulk, with only a minor contribution from the more resistive surface depletion layer, caused by electron donation into the SnO. In smaller particles/high surface areas, this conduction is dominated by the depletion layer, either by narrowing the bulk area or by complete depletion. This effect is exaggerated in the (101) plane due to its smaller dimension, resulting in effective depletion layer formation, and the granular network morphology ensuring conduction must be mediated through interfaces between (101) planes.

To examine the proposed adsorption/charge exchange-based mechanism in more detail, density functional theory (DFT) calculations of the interaction of analyte gases and SnO surfaces were performed. As SnO is a layered material, surface models of the top nanoflower surface, dominated by the (001) plane, and the nanoflower edges, dominated by the (101) plane, are studied. Interaction energies and the computed net Bader charge on Sn for each analyte-surface combination are presented in Table 3.

Table 3 Computed interaction energies and net Bader charge exchange for VOC analytes and water on SnO (001) and (101) surfaces

			SnO (001)			
	Surface	**Methanol**	**Ethanol**	**Isopropanol**	**Acetone**	**Water**
Δ E (eV/molecule)	-	-0.29	-0.37	-0.45	-0.41	-0.43
Sn net charge / electrons	2.6	2.4-2.6	2.4-2.6	2.5-2.6	2.5-2.6	2.4-2.6
	Surface	**Methanol**	**Ethanol**	**Isopropanol**	**Acetone**	**Water**
			SnO (101)			
Δ E (eV/molecule)	-	-0.78	-0.64	-0.65	-0.35	-0.50
Sn net charge / electrons	2.3-2.4	2.3-2.8	2.5-2.9	2.5-3.2	2.7-3.6	2.5-3.0

Based on the calculated interaction energies all species are expected to interact sufficiently at SnO surfaces at room temperature, with the smallest ΔE being -0.29 eV. The range of interaction energies for the analytes are consistent with the sensing ability of SnO, given that they are not so large as to indicate strong adsorption and not so weak that there is no interaction with the surface. No clear single interaction site can be seen in the atomic structures shown in Fig.9 which is consistent with the magnitude of the interaction energies. There appears to be a preference on both surfaces for the alcohol hydroxyl group and the carbonyl of acetone to be directed to the surface**.** Therefore the observed humidity independence of the measurements can be explained by our computed interaction energies that indicate no clear preference for water adsorption and water molecules can be displaced by the analyte molecule. The energies and structures can also suggest that water and the analytes will not compete for the same site. Conversely, the computed adsorption energy of water (-0.43 eV/molecule) and its high abundance during the vent can facilitate scouring the surface of other analytes by displacing these species. The larger interaction energy of IPA (-0.45 eV), could partly explain the incomplete removal behavior of IPA shown in Fig. 8a. This can also be caused by IPA being the reaction solvent, which could stabilize the SnO (001) plane and promote preferential IPA binding sites [87].

Different surfaces offer different interaction environments for adsorbing species. The (101) surface shows larger interaction energies than the (001) surface for all species, except acetone. This enhancement is larger for the smaller molecules, e.g. -0.78 vs. -0.29 eV for methanol and -0.65 vs. -0.45 eV for IPA, which is likely associated with the greater steric hindrance of the larger groups, limiting their access to the inter-sheet region. The surface orientation dependence of the interaction energies means that the sensing response of SnO will be dependent on the contributions of the ensemble of planes involved and this can be useful in motivating further work to control the dominant surface facet of nanostructured SnO.

The band gap of the SnO (101) surface was estimated from the valence to conduction band energy difference in the density of states (DOS) and is *ca.* 1 eV. This energy gap persists after the organic molecules and water interact at the surface, further indicating a non-chemisorption interaction. Typical atomic charges, computed from the Bader partitioning scheme [115], for Sn in the (101) surface layer and the sub-surface layer are 2.4 and 2.3-2.4 electrons respectively. Upon interacting with all molecules, Table 3, the charge of the top layer Sn atoms increases to 2.5-3.6

electrons. This indicates a partial oxidation of surface-terminating Sn species as a result of interactions with the hydroxyl or carbonyl sites. As SnO is a p-type semiconductor, this would increase the resistance due to the associated elimination of hole charge carriers caused by the charge donation when this surface is exposed. By contrast on the (001) surface the change in Sn charges is negligible which is consistent with the weaker interactions between the molecules and this surface. This suggests that the sensing is dominated by the more reactive (101) surface. As already outlined, due to the sparse granular network, the conduction profile is dominated by a series of bottleneck regions of (101) plane interfaces that effectively modulate conduction amplifying the response.

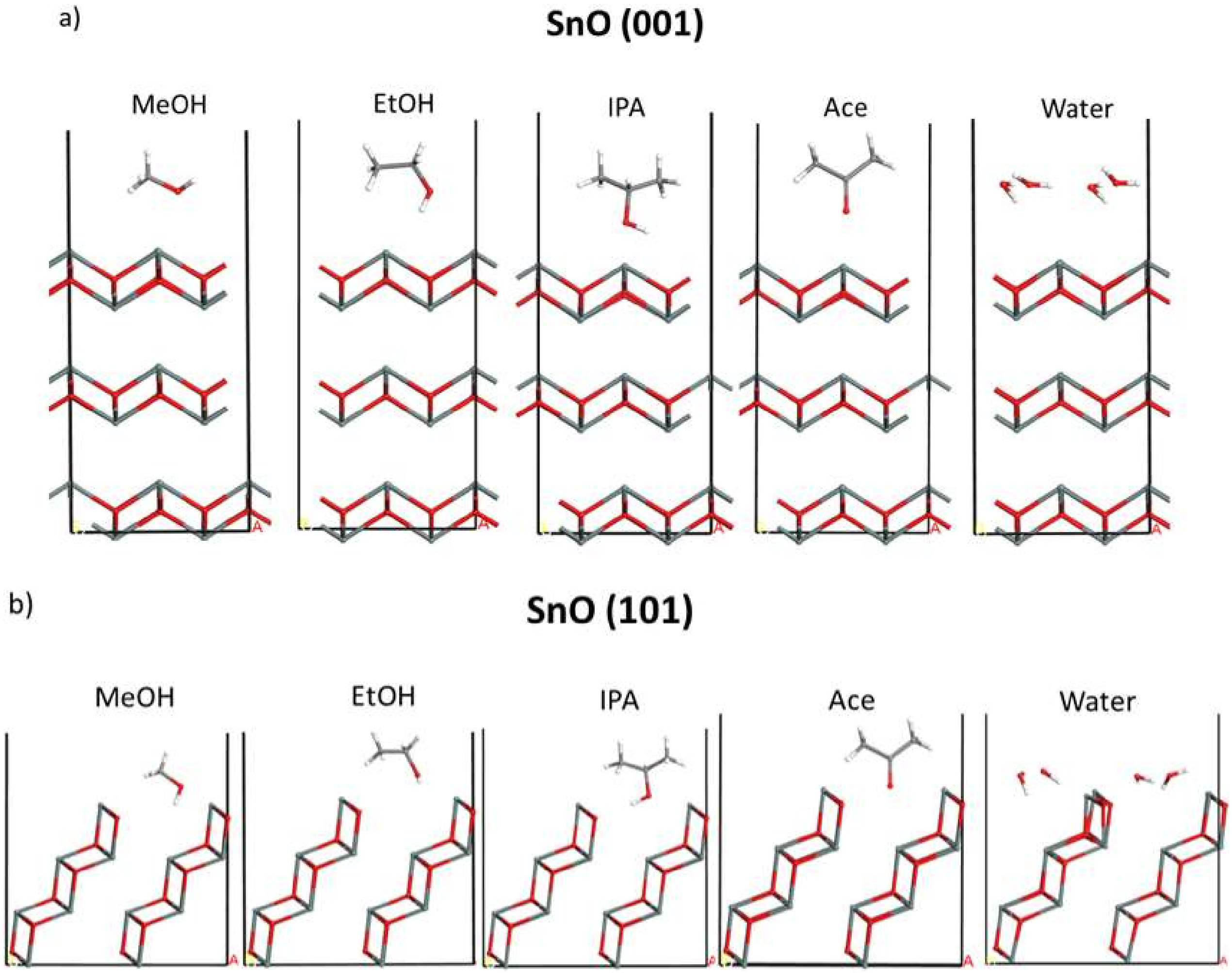

Figure 9 Optimised atomic structures of MeOH, EtOH, IPA, Ace and H_2O on SnO (001) and (101) surfaces. Colour scheme: tin: dark grey, carbon: light grey, oxygen: red and hydrogen: white.

The resource-efficient hybrid LIG-SnO VOC sensors presented here demonstrate good sensitivity and stability under ambient conditions. They share the selectivity challenges common to all chemiresistive MOX sensors fabricated using pristine or undecorated MOX particles. However, reported literature methods to improve selectivity in chemiresistive MOX sensors (including co-deposition and decoration with noble metals) are resource-intensive and present sustainability challenges [56,58,116]. Considering future resource-efficient methods to improve selectivity for our LIG-SnO devices, *Jaśkaniec et al.* observed that the choice of reflux solvent and temperature determine the morphology of this family of SnO nanoparticles [89]. For example, butanol reflux led to cubic platelets instead of the nanoflowers produced from IPA reflux. Using distinct SnO particle morphologies to create SnO-LIG sensing elements with known cross-selectivity behavior could enable orthogonal sensing approaches based on multi-sensor arrays on a single substrate. Such sensor arrays, integrated with a machine learning layer [117,118], could fingerprint the interaction matrix to enable selective identification, and thus accurate concentration estimation for VOCs.

Conclusion

We report a resource-efficient hybrid SnO nanoflower-Laser-Induced Graphitic carbon (LIG) chemiresistive sensor platform for VOC headspace sensing at ambient temperature. This early demonstration of SnO nanoflowers as VOC-sensitive MOX nanomaterials also features additive integration at low mass-loadings with direct-written laser-graphitized 3D porous carbon contact electrodes. The SnO-LIG sensors demonstrate responses characteristic of p-type semiconductors, with increases in device resistance when exposed to methanol headspace vapor (~5% at 150 ppm, ~35% at 4100 ppm) or other reducing VOCs in a versatile, low-cost custom chamber. Density functional theory simulations provide key information on the interaction of VOC molecules and water at SnO surfaces with different surface orientations. The (101) surface shows stronger, but still not chemisorbed, interaction energies and a notable oxidation of surface tin sites, whereas the (001) surface has weaker interactions with molecular species and no change in Sn oxidation state.

A limit of detection of 170±40 ppm was demonstrated for methanol, below 8-hour workplace safety exposure limits (200 ppm). Rapid response times (t_{90}=35 s @150 ppm methanol, 5 s recovery) and stability > 21 days were demonstrated, competitive with existing resource-intensive chemiresistive MOX sensors [27,60,119]. These resource- and energy-efficient room-temperature chemiresistive SnO-LIG VOC sensors show significant potential for integration as low-power sensors for future wearable worker safety sensors or Edge-IoT applications [120].

Acknowledgements

We are grateful to Dr. Emanuele Pelucchi for training and guidance on x-ray diffraction measurements. This publication has emanated from research conducted with the financial support of Science Foundation Ireland (SFI) under Grant Nos. SFI 16/RC/3918 (CONFIRM) and 13/RC/2077 (CONNECT), cofunded by the European Regional Development Fund; and by the European Union's Horizon 2020 research and innovation program under Grant Agreement No. 814496 (APACHE); and European Union H2020 project Greenart (101060941) project.

1. References

[1] L.A. Wallace, E. Pellizzari, B. Leaderer, H. Zelon, L. Sheldon, Emissions of volatile organic compounds from building materials and consumer products, Atmospheric Environment (1967). 21 (1987) 385–393. https://doi.org/10.1016/0004-6981(87)90017-5.

[2] G. Wieslander, D. Norbäck, E. Björnsson, C. Janson, G. Boman, Asthma and the indoor environment: the significance of emission of formaldehyde and volatile organic compounds from newly painted indoor surfaces, Int Arch Occup Environ Health. 69 (1997) 115–124. https://doi.org/10.1007/S004200050125.

[3] S. Batterman, C. Jia, G. Hatzivasilis, Migration of volatile organic compounds from attached garages to residences: A major exposure source, Environ Res. 104 (2007) 224–240. https://doi.org/10.1016/J.ENVRES.2007.01.008.

[4] A.L. Clobes, G.P. Ananth, A.L. Hood, J.A. Schroeder, K.A. Lee, Human Activities as Sources of Volatile Organic Compounds in Residential Environments, Ann N Y Acad Sci. 641 (1992) 79–86. https://doi.org/10.1111/j.1749-6632.1992.tb16534.x.

[5] G. Wieslander, D. Norbäck, E. Björnsson, C. Janson, G. Boman, Asthma and the indoor environment: The significance of emission of formaldehyde and volatile organic compounds from newly painted indoor surfaces, Int Arch Occup Environ Health. 69 (1996) 115–124. https://doi.org/10.1007/s004200050125.

[6] Q. He, Y. Yan, H. Li, Y. Zhang, L. Chen, Y. Wang, Characteristics and reactivity of volatile organic compounds from non-coal emission sources in China, Atmos Environ. 115 (2015) 153–162. https://doi.org/10.1016/j.atmosenv.2015.05.066.

[7] Q. Lin, Z. Gao, W. Zhu, J. Chen, T. An, Underestimated contribution of fugitive emission to VOCs in pharmaceutical industry based on pollution characteristics, odorous activity and health risk assessment, J Environ Sci (China). 126 (2022) 722–733. https://doi.org/10.1016/j.jes.2022.03.005.

[8] L. Zhang, J. Wang, X. Hu, J. Zhou, M. Zhao, J. Zhang, Y. Bo, Y. Huang, Y. Zhang, VOCs and PM concentrations in underground parking garages of the commercial center and high-rise residential buildings, Air Qual Atmos Health. 14 (2021) 1117–1131. https://doi.org/10.1007/S11869-021-01003-Z/FIGURES/7.

[9] U. Schlink, M. Rehwagen, M. Damm, M. Richter, M. Borte, O. Herbarth, Seasonal cycle of indoor-VOCs: Comparison of apartments and cities, Atmos Environ. 38 (2004) 1181–1190. https://doi.org/10.1016/J.ATMOSENV.2003.11.003.

[10] Division of Criteria Documentation and Standards, National Institute for Occupational Safety and Health (NIOSH), Occupational Exposure to Methyl Alcohol, Criteria for a Recommended Standard. (1976). https://www.cdc.gov/niosh/docs/76-148/.

[11] NIOSH, Methanol manipulation.pdf, (1978).

[12] AEGL (Subcommittee on Acute Exposure Guideline Levels), Acute Exposure Guideline Levels (AEGLs) for Methanol - Interim, (2005).

[13] J.E. Cometto-Muñiz, W.S. Cain, Thresholds for odor and nasal pungency, Physiol Behav. 48 (1990) 719–725. https://doi.org/10.1016/0031-9384(90)90217-R.

[14] G.A. Blengini, C.E.L. Latunussa, U. Eynard, C. Torres de Matos, D. Wittmer, K. Georgitzikis, C. Pavel, S. Carrara, L. Mancini, M. Unguru, D. Blagoeva, F. Mathieux, D. Pennington, Study on the EU's list of Critical Raw Materials (2020) Final Report, 2020. https://doi.org/10.2873/904613.

[15] Z. Wang, A. Ali Haidry, L. Xie, A. Zavabeti, Z. Li, W. Yin, R. Lontio Fomekong, B. Saruhan, Acetone sensing applications of Ag modified TiO2 porous nanoparticles synthesized via facile hydrothermal method, Appl Surf Sci. 533 (2020) 147383. https://doi.org/10.1016/j.apsusc.2020.147383.

[16] J. Bai, B. Zhou, Titanium dioxide nanomaterials for sensor applications, Chem Rev. 114 (2014) 10131–10176. https://doi.org/10.1021/cr400625j.

[17] T. Seiyama, K. Fujiishi, M. Nagatani, A. Kato, A New Detector for Gaseous Components Using Zinc Oxide Thin Films, The Journal of the Society of Chemical Industry, Japan. 66 (1963) 652–655. https://doi.org/10.1246/nikkashi1898.66.5_652.

[18] P.J. Shaver, Activated tungsten oxide gas detectors, Appl Phys Lett. 11 (1967) 255–257. https://doi.org/10.1063/1.1755123.

[19] T. Seiyama, A. Kato, K. Fujiishi, M. Nagatani, A New Detector for Gaseous Components Using Semiconductive Thin Films, Anal Chem. 34 (1962) 1502–1503. https://doi.org/10.1021/ac60191a001.

[20] N. Yamazoe, J. Fuchigami, M. Kishikawa, T. Seiyama, Interactions of tin oxide surface with O2, H2O AND H2, Surf Sci. 86 (1979) 335–344. https://doi.org/10.1016/0039-6028(79)90411-4.

[21] P.T. Moseley, D.E. Williams, A selective ammonia sensor, Sens Actuators B Chem. 1 (1990) 113–115. https://doi.org/10.1016/0925-4005(90)80183-Z.

[22] S.J. Kim, I.S. Hwang, C.W. Na, I.D. Kim, Y.C. Kang, J.H. Lee, Ultrasensitive and selective C2H5OH sensors using Rh-loaded In2O3 hollow spheres, J Mater Chem. 21 (2011) 18560–18567. https://doi.org/10.1039/c1jm14252f.

[23] J.W. Yoon, J.K. Choi, J.H. Lee, Design of a highly sensitive and selective C 2H 5OH sensor using p-type Co 3O 4 nanofibers, Sens Actuators B Chem. 161 (2012) 570–577. https://doi.org/10.1016/J.SNB.2011.11.002.

[24] M. Hübner, C.E. Simion, A. Tomescu-Stănoiu, S. Pokhrel, N. Bârsan, U. Weimar, Influence of humidity on CO sensing with p-type CuO thick film gas sensors, Sens Actuators B Chem. 153 (2011) 347–353. https://doi.org/10.1016/J.SNB.2010.10.046.

[25] S. Pokhrel, C.E. Simion, V. Quemener, N. Bârsan, U. Weimar, Investigations of conduction mechanism in Cr2O3 gas sensing thick films by ac impedance spectroscopy and work function changes measurements, Sens Actuators B Chem. 133 (2008) 78–83. https://doi.org/10.1016/J.SNB.2008.01.054.

[26] C. Wang, J. Liu, Q. Yang, P. Sun, Y. Gao, F. Liu, J. Zheng, G. Lu, Ultrasensitive and low detection limit of acetone gas sensor based on W-doped NiO hierarchical nanostructure, Sens Actuators B Chem. 220 (2015) 59–67. https://doi.org/10.1016/J.SNB.2015.05.037.

[27] X. Yang, H. Fu, L. Zhang, X. An, S. Xiong, X. Jiang, A. Yu, Enhanced gas sensing performance based on the fabrication of polycrystalline Ag@TiO2 core-shell nanowires, Sens Actuators B Chem. 286 (2019) 483–492. https://doi.org/10.1016/j.snb.2019.01.096.

[28] X.H. Yang, H.T. Fu, K. Wong, X.C. Jiang, A.B. Yu, Experimental and theoretical studies of V2O5@TiO2 core-shell hybrid composites with high gas sensing performance towards ammonia, Nanotechnology. 24 (2013) 103–115. https://doi.org/10.1016/j.snb.2017.05.027.

[29] X. Xing, N. Chen, Y. Yang, R. Zhao, Z. Wang, Z. Wang, T. Zou, Y. Wang, Pt-Functionalized Nanoporous TiO2 Nanoparticles With Enhanced Gas Sensing Performances Toward Acetone, Physica Status Solidi (A) Applications and Materials Science. 215 (2018). https://doi.org/10.1002/PSSA.201800100.

[30] P.K. Dutta, A. Ginwalla, B. Hogg, B.R. Patton, B. Chwieroth, Z. Liang, P. Gouma, M. Mills, S. Akbar, Interaction of carbon monoxide with anatase surfaces at high temperatures: Optimization of a carbon monoxide sensor, Journal of Physical Chemistry B. 103 (1999) 4412–4422. https://doi.org/10.1021/jp9844718.

[31] C. Imawan, F. Solzbacher, H. Steffes, E. Obermeier, Gas-sensing characteristics of modified-MoO3 thin films using Ti-overlayers for NH3 gas sensors, Sens Actuators B Chem. 64 (2000) 193–197. https://doi.org/10.1016/S0925-4005(99)00506-7.

[32] C. Wang, X. Cheng, X. Zhou, P. Sun, X. Hu, K. Shimanoe, G. Lu, N. Yamazoe, Hierarchical α-Fe2O3/NiO composites with a hollow structure for a gas sensor, ACS Appl Mater Interfaces. 6 (2014) 12031–12037. https://doi.org/10.1021/am501063z.

[33] X. Li, J. Liu, H. Guo, X. Zhou, C. Wang, P. Sun, X. Hu, G. Lu, Au@In2O3 core–shell composites: a metal–semiconductor heterostructure for gas sensing applications, RSC Adv. 5 (2014) 545–551. https://doi.org/10.1039/C4RA12467G.

[34] M. Kugishima, K. Shimanoe, N. Yamazoe, C2H4O sensing properties for thick film sensor using La2O3-modified SnO2, Sens Actuators B Chem. 118 (2006) 171–176. https://doi.org/10.1016/J.SNB.2006.04.053.

[35] N. Barsan, C. Simion, T. Heine, S. Pokhrel, U. Weimar, Modeling of sensing and transduction for p-type semiconducting metal oxide based gas sensors, J Electroceram. 25 (2010) 11–19. https://doi.org/10.1007/s10832-009-9583-x.

[36] J.W. Yoon, H.J. Kim, I.D. Kim, J.H. Lee, Electronic sensitization of the response to C2H5OH of p-type NiO nanofibers by Fe doping, Nanotechnology. 24 (2013). https://doi.org/10.1088/0957-4484/24/44/444005.

[37] N. Barsan, U. Weimar, Conduction model of metal oxide gas sensors, J Electroceram. 7 (2001) 143–167. https://doi.org/10.1023/A:1014405811371.

[38] Zheng Wei Pan, Zu Rong Dai, Zhong Lin Wang, Nanobelts of semiconducting oxides, Science (1979). 291 (2001) 1947–1949. https://doi.org/10.1126/SCIENCE.1058120.

[39] M. Law, H. Kind, B. Messer, F. Kim, P. Yang, Photochemical Sensing of NO 2 with SnO 2 Nanoribbon Nanosensors at Room Temperature**, Angew. Chem. Int. Ed. 41 (2002). https://doi.org/10.1002/1521-3773(20020703)41:13<2405::AID-ANIE2405>3.0.CO;2-3.

[40] E. Comini, G. Faglia, G. Sberveglieri, Stable and highly sensitive gas sensors based on semiconducting oxide nanobelts, Appl. Phys. Lett. 81 (2002) 1869. https://doi.org/10.1063/1.1504867.

[41] S.J. Kim, I.S. Hwang, J.K. Choi, Y.C. Kang, J.H. Lee, Enhanced C2H5OH sensing characteristics of nano-porous In2O3 hollow spheres prepared by sucrose-mediated hydrothermal reaction, Sens Actuators B Chem. 155 (2011) 512–518. https://doi.org/10.1016/J.SNB.2010.12.055.

[42] F. Gyger, M. H€, C. Feldmann, N. Barsan, U. Weimar, Nanoscale SnO 2 Hollow Spheres and Their Application as a Gas-Sensing Material, Chem. Mater. 22 (2010) 4821. https://doi.org/10.1021/cm1011235.

[43] Z. Zhong, Y. Yin, B. Gates, Y. Xia, Preparation of mesoscale hollow spheres of TiO2 and SnO2 by templating against crystalline arrays of polystyrene beads, Advanced Materials. 12 (2000) 206–209. https://doi.org/10.1002/(SICI)1521-4095(200002)12:3<206::AID-ADMA206>3.0.CO;2-5.

[44] J.H. Lee, Gas sensors using hierarchical and hollow oxide nanostructures: Overview, Sens Actuators B Chem. 140 (2009) 319–336. https://doi.org/10.1016/J.SNB.2009.04.026.

[45] A. Kolmakov, M. Moskovits, CHEMICAL SENSING AND CATALYSIS BY ONE-DIMENSIONAL METAL-OXIDE NANOSTRUCTURES, Annu. Rev. Mater. Res. 34 (2004) 151–80. https://doi.org/10.1146/annurev.matsci.34.040203.112141.

[46] P.T. Moseley, Solid state gas sensors, Meas Sci Technol. 8 (1997) 223–237. https://doi.org/10.1088/0957-0233/8/3/003.

[47] N. Yamazoe, K. Shimanoe, New perspectives of gas sensor technology, Sens Actuators B Chem. 138 (2009) 100–107. https://doi.org/10.1016/J.SNB.2009.01.023.

[48] N. Barsan, C. Simion, T. Heine, S. Pokhrel, U. Weimar, Modeling of sensing and transduction for p-type semiconducting metal oxide based gas sensors, J Electroceram. 25 (2010) 11–19. https://doi.org/10.1007/s10832-009-9583-x.

[49] G.C. Bond, L.R. Molloy, M.J. Fuller, Oxidation of carbon monoxide over palladium-tin(IV) oxide catalysts: An example of spillover catalysis, J Chem Soc Chem Commun. (1975) 796–797. https://doi.org/10.1039/C39750000796.

[50] K. Großmann, S. Wicker, U. Weimar, N. Barsan, Impact of Pt additivies on the surface reactions between SnO2, water vapour, CO and H2; an operando investigation, Phys. Chem. Chem. Phys. 15 (2013) 19151–19158. https://doi.org/10.1039/c3cp52782d.

[51] T. Seiyama, S. Kagawa, Study on a Detector for Gaseous Components Using Semiconductive Thin Films, Anal Chem. 38 (1966) 1069–1073. https://doi.org/10.1021/ac60240a031.

[52] N. Murata, T. Suzuki, M. Kobayashi, F. Togoh, K. Asakura, Characterisation of Pt-doped SnO2 catalyst for a high-performance micro gas sensor, Phys. Chem. Chem. Phys. 15 (2013) 17938. https://doi.org/10.1039/c3cp52490f.

[53] T. Suzuki, S. Soma, T. Nagase, Methane Sensor for Cordless Utility Gas Alarms, Fuji Electric Review. 84 (2012) 278–282.

[54] N. Yamazoe, Y. Kurokawa, T. Seiyama, Effects of additives on semiconductor gas sensors, Sensors and Actuators. 4 (1983) 283–289. https://doi.org/10.1016/0250-6874(83)85034-3.

[55] D. Degler, H.W. Pereira De Carvalho, K. Kvashnina, J.D. Grunwaldt, U. Weimar, N. Barsan, Structure and chemistry of surface-doped Pt:SnO2 gas sensing materials, RSC Adv. 6 (2016) 28149–28155. https://doi.org/10.1039/c5ra26302f.

[56] D. Degler, S. Rank, S. Müller, H.W. Pereira De Carvalho, J.D. Grunwaldt, U. Weimar, N. Barsan, Gold-Loaded Tin Dioxide Gas Sensing Materials: Mechanistic Insights and the Role of Gold Dispersion, ACS Sens. 1 (2016) 1322–1329. https://doi.org/10.1021/acssensors.6b00477.

[57] D. Degler, S.A. Müller, D.E. Doronkin, D. Wang, J.D. Grunwaldt, U. Weimar, N. Barsan, Platinum loaded tin dioxide: A model system for unravelling the interplay between heterogeneous catalysis and gas sensing, J Mater Chem A Mater. 6 (2018) 2034–2046. https://doi.org/10.1039/c7ta08781k.

[58] M. Hübner, N. Bârsan, U. Weimar, Influences of Al, Pd and Pt additives on the conduction mechanism as well as the surface and bulk properties of SnO2 based polycrystalline thick film gas sensors, Sens Actuators B Chem. 171–172 (2012) 172–180. https://doi.org/10.1016/J.SNB.2012.02.080.

[59] M. Epifani, S. Kaciulis, A. Mezzi, T. Zhang, J. Arbiol, P. Siciliano, A. Landström, I. Concina, A. Moumen, E. Comini, C. Xiangfeng, Rhodium as efficient additive for boosting acetone sensing by TiO2 nanocrystals. Beyond the classical view of noble metal additives, Sens Actuators B Chem. 319 (2020). https://doi.org/10.1016/j.snb.2020.128338.

[60] H. Fu, X. Yang, X. An, W. Fan, X. Jiang, A. Yu, Experimental and theoretical studies of V2O5@TiO2 core-shell hybrid composites with high gas sensing performance towards ammonia, Sens Actuators B Chem. 252 (2017) 103–115. https://doi.org/10.1016/j.snb.2017.05.027.

[61] A. Wisitsoraat, A. Tuantranont, E. Comini, G. Sberveglieri, W. Wlodarski, Characterization of n-type and p-type semiconductor gas sensors based on NiOx doped TiO2 thin films, Thin Solid Films. 517 (2009) 2775–2780. https://doi.org/10.1016/j.tsf.2008.10.090.

[62] H.I. Kwon, Low-temperature-operated sensitive NO2gas sensors based on p-type SnO thin-film and thin-film transistors, Proceedings of AM-FPD 2020 - 27th International Workshop on Active-Matrix Flatpanel Displays and Devices: TFT Technologies and FPD Materials. (2020) 55–58. https://doi.org/10.23919/AM-FPD49417.2020.9224482.

[63] J. Wang, P. Yang, X. Wei, High-performance, room-temperature, and no-humidity-impact ammonia sensor based on heterogeneous nickel oxide and zinc oxide nanocrystals, ACS Appl Mater Interfaces. 7 (2015) 3816–3824. https://doi.org/10.1021/am508807a.

[64] J. Lin, Z. Peng, Y. Liu, F. Ruiz-Zepeda, R. Ye, E.L.G. Samuel, M.J. Yacaman, B.I. Yakobson, J.M. Tour, Laser-induced porous graphene films from commercial polymers, Nat Commun. 5 (2014) 5714. https://doi.org/10.1038/ncomms6714.

[65] Y. Dong, S.C. Rismiller, J. Lin, Molecular dynamic simulation of layered graphene clusters formation from polyimides under extreme conditions, Carbon N Y. 104 (2016) 47–55. https://doi.org/10.1016/j.carbon.2016.03.050.

[66] R. Murray, M. Burke, D. Iacopino, A.J. Quinn, Design of Experiments and Optimization of Laser-Induced Graphene, ACS Omega. 6 (2021) 16736–16743. https://doi.org/10.1021/acsomega.1c00309.

[67] Hassan Hamidi, Juliette Levieux, Cathal Larrigy, Alida Russo, Eoghan Vaughan, Richard Murray, Aidan J. Quinn, Daniela Iacopino, Laser induced graphene (LIG) biosensors derived from chitosan: towards sustainable and green electronics, Biosens Bioelectron X. 11 (2020) 826–835. https://doi.org/10.1016/j.biosx.2023.100403.

[68] D. Iacopino, E. Vaughan, C. Larrigy, M. Burke, L. Sygellou, A.J. Quinn, C. Galiotis, Visible laser scribing fabrication of porous graphitic carbon electrodes: Morphologies, electrochemical properties, and applications as disposable sensor platforms, ACS Appl Electron Mater. 2 (2020) 3279–3288. https://doi.org/10.1021/acsaelm.0c00612.

[69] A. Imbrogno, J. Islam, C. Santillo, R. Castaldo, L. Sygellou, C. Larrigy, R. Murray, E. Vaughan, M.K. Hoque, A.J. Quinn, D. Iacopino, Laser-Induced Graphene Supercapacitors by Direct Laser Writing of Cork Natural Substrates, ACS Appl Electron Mater. 4 (2022) 1541–1551. https://doi.org/10.1021/acsaelm.1c01202.

[70] R. Murray, O. O'Neill, E. Vaughan, D. Iacopino, A. Blake, C. Lyons, D. O'Connell, J. O'Brien, A.J. Quinn, Direct-write formation of integrated bottom contacts to laser-induced graphene-like carbon, Nanotechnology. 33 (2022). https://doi.org/10.1088/1361-6528/ac7c7b.

[71] Z. Peng, L.Q. Tao, S. Zou, C. Zhu, G. Wang, H. Sun, T.L. Ren, A Multi-functional NO2 gas monitor and Self-Alarm based on Laser-Induced graphene, Chemical Engineering Journal. 428 (2022) 131079. https://doi.org/10.1016/j.cej.2021.131079.

[72] W. Yan, W. Yan, T. Chen, J. Xu, Q. Tian, D. Ho, Size-Tunable Flowerlike MoS2Nanospheres Combined with Laser-Induced Graphene Electrodes for NO2Sensing, ACS Appl Nano Mater. 3 (2020) 2545–2553. https://doi.org/10.1021/acsanm.9b02614.

[73] L. Yang, N. Yi, J. Zhu, Z. Cheng, X. Yin, X. Zhang, H. Zhu, H. Cheng, Novel gas sensing platform based on a stretchable laser-induced graphene pattern with self-heating capabilities, J Mater Chem A Mater. 8 (2020) 6487–6500. https://doi.org/10.1039/c9ta07855j.

[74] L. Yang, G. Zheng, Y. Cao, C. Meng, Y. Li, H. Ji, X. Chen, G. Niu, J. Yan, Y. Xue, H. Cheng, Moisture-resistant, stretchable NOx gas sensors based on laser-induced graphene for environmental monitoring and breath analysis, Microsyst Nanoeng. 8 (2022). https://doi.org/10.1038/s41378-022-00414-x.

[75] R. Ye, Y. Chyan, J. Zhang, Y. Li, X. Han, C. Kittrell, J.M. Tour, Laser-Induced Graphene Formation on Wood, Advanced Materials. 29 (2017) 1702211. https://doi.org/10.1002/ADMA.201702211.

[76] R. Ye, D.K. James, J.M. Tour, Laser-Induced Graphene, Acc Chem Res. 51 (2018) 1609–1620. https://doi.org/10.1021/acs.accounts.8b00084.

[77] C. Larrigy, M. Burke, A. Imbrogno, E. Vaughan, C. Santillo, M. Lavorgna, L. Sygellou, G. Paterakis, C. Galiotis, D. Iacopino, A.J. Quinn, Porous 3D Graphene from Sustainable Materials: Laser Graphitization of Chitosan, Adv Mater Technol. 2201228 (2022). https://doi.org/10.1002/admt.202201228.

[78] M. Burke, C. Larrigy, E. Vaughan, G. Paterakis, L. Sygellou, A.J. Quinn, G. Herzog, C. Galiotis, D. Iacopino, Fabrication and Electrochemical Properties of Three-Dimensional (3D) Porous Graphitic and Graphenelike Electrodes Obtained by Low-Cost Direct Laser Writing Methods, ACS Omega. 5 (2020) 1540–1548. https://doi.org/10.1021/acsomega.9b03418.

[79] G.W. Watson, Origin of the electron distribution in SnO, Journal of Chemical Physics. 114 (2001) 758–763. https://doi.org/10.1063/1.1331102.

[80] J.P. Allen, D.O. Scanlon, S.C. Parker, G.W. Watson, Tin monoxide: Structural prediction from first principles calculations with van der Waals corrections, Journal of Physical Chemistry C. 115 (2011) 19916–19924. https://doi.org/10.1021/JP205148Y/ASSET/IMAGES/LARGE/JP-2011-05148Y_0004.JPEG.

[81] P.H. Suman, A.A. Felix, H.L. Tuller, J.A. Varela, M.O. Orlandi, Comparative gas sensor response of SnO 2 , SnO and Sn 3 O 4 nanobelts to NO 2 and potential interferents, Sensors and Actuators B. 208 (2015) 122–127. https://doi.org/10.1016/j.snb.2014.10.119.

[82] A. Togo, F. Oba, I. Tanaka, K. Tatsumi, First-principles calculations of native defects in tin monoxide, Phys Rev B Condens Matter Mater Phys. 74 (2006) 1–8. https://doi.org/10.1103/PhysRevB.74.195128.

[83] F. Oba, M. Choi, A. Togo, A. Seko, I. Tanaka, Native defects in oxide semiconductors: A density functional approach, Journal of Physics Condensed Matter. 22 (2010). https://doi.org/10.1088/0953-8984/22/38/384211.

[84] Z.R. Dai, Z.W. Pan, Z.L. Wang, Growth and structure evolution of novel tin oxide diskettes, J Am Chem Soc. 124 (2002) 8673–8680. https://doi.org/10.1021/ja026262d.

[85] H. Wang, Y. Wang, J. Xu, H. Yang, C.-S. Lee, A.L. Rogach, Polyvinylpyrrolidone-Assisted Ultrasonic Synthesis of SnO Nanosheets and Their Use as Conformal Templates for Tin Dioxide Nanostructures, (2012). https://doi.org/10.1021/la301827p.

[86] H.S. Jeong, M.J. Park, S.H. Kwon, H.J. Joo, S.H. Song, H.I. Kwon, Low temperature NO2 sensing properties of RF-sputtered SnO-SnO2 heterojunction thin-film with p-type semiconducting behavior, Ceram Int. 44 (2018) 17283–17289. https://doi.org/10.1016/j.ceramint.2018.06.189.

[87] Q. Ren, X. Zhang, Y. Wang, M. Xu, J. Wang, Q. Tian, K. Jia, X. Liu, Y. Sui, C. Liu, J. Yun, J. Yan, W. Zhao, Z. Zhang, Shape-controlled and stable hollow frame structures of SnO and their highly sensitive NO2 gas sensing, Sens Actuators B Chem. 340 (2021) 129940. https://doi.org/10.1016/j.snb.2021.129940.

[88] F. Zhang, J. Zhu, D. Zhang, U. Schwingenschlögl, H.N. Alshareef, Two-Dimensional SnO Anodes with a Tunable Number of Atomic Layers for Sodium Ion Batteries, Nano Lett. 17 (2017) 1302–1311. https://doi.org/10.1021/acs.nanolett.6b05280.

[89] S. Jaśkaniec, S.R. Kavanagh, J. Coelho, S. Ryan, C. Hobbs, A. Walsh, D.O. Scanlon, V. Nicolosi, Solvent engineered synthesis of layered SnO for high-performance anodes, Npj 2D Materials and Applications 2021 5:1. 5 (2021) 1–9. https://doi.org/10.1038/s41699-021-00208-1.

[90] H. Uchiyama, E. Hosono, I. Honma, H. Zhou, H. Imai, A nanoscale meshed electrode of single-crystalline SnO for lithium-ion rechargeable batteries, (2007). https://doi.org/10.1016/j.elecom.2007.10.018.

[91] B. Kumar, D.H. Lee, S.H. Kim, B. Yang, S. Maeng, S.W. Kim, General route to single-crystalline SnO nanosheets on arbitrary substrates, Journal of Physical Chemistry C. 114 (2010) 11050–11055. https://doi.org/10.1021/jp101682v.

[92] M.O. Orlandi, E.R. Leite, R. Aguiar, J. Bettini, E. Longo, Growth of SnO Nanobelts and Dendrites by a Self-Catalytic VLS Process, (2006). https://doi.org/10.1021/jp057099m.

[93] M.Z. Iqbal, F. Wang, T. Feng, H. Zhao, M.Y. Rafique, Rafi Ud Din, M.H. Farooq, Q.U.A. Javed, D.F. Khan, Facile synthesis of self-assembled SnO nano-square sheets and hydrogen absorption characteristics, Mater Res Bull. 47 (2012) 3902–3907. https://doi.org/10.1016/j.materresbull.2012.07.002.

[94] H. Uchiyama, S. Nakanishi, H. Kozuka, Hydrothermal synthesis of nanostructured SnO particles through crystal growth in the presence of gelatin, J Solid State Chem. 217 (2014) 87–91. https://doi.org/10.1016/j.jssc.2014.05.023.

[95] L. Wang, H. Ji, F. Zhu, Z. Chen, Y. Yang, X. Jiang, J. Pinto, G. Yang, Large-scale preparation of shape controlled SnO and improved capacitance for supercapacitors: From nanoclusters to square microplates, Nanoscale. 5 (2013) 7613–7621. https://doi.org/10.1039/c3nr00951c.

[96] D. Aurbach, A. Nimberger, B. Markovsky, E. Levi, E. Sominski, A. Gedanken, Nanoparticles of SnO Produced by Sonochemistry as Anode Materials for Rechargeable Lithium Batteries, (2002). https://doi.org/10.1021/cm021137m.

[97] T. Krishnakumar, N. Pinna, K.P. Kumari, K. Perumal, R. Jayaprakash, Microwave-assisted synthesis and characterization of tin oxide nanoparticles, Mater Lett. 62 (2008) 3437–3440. https://doi.org/10.1016/J.MATLET.2008.02.062.

[98] D.S. Wu, C.Y. Han, S.Y. Wang, N.L. Wu, I.A. Rusakova, Microwave-assisted solution synthesis of SnO nanocrystallites, Mater Lett. 53 (2002) 155–159. https://doi.org/10.1016/S0167-577X(01)00468-2.

[99] V.X. Hien, J.H. Lee, J.J. Kim, Y.W. Heo, Structure and NH3 sensing properties of SnO thin film deposited by RF magnetron sputtering, Sens Actuators B Chem. 194 (2014) 134–141. https://doi.org/10.1016/j.snb.2013.12.086.

[100] V.X. Hien, Y.W. Heo, Effects of violet-, green-, and red-laser illumination on gas-sensing properties of SnO thin film, Sens Actuators B Chem. 228 (2016) 185–191. https://doi.org/10.1016/j.snb.2015.12.105.

[101] Q. Ren, X. Zhang, Y. Guo, M. Xu, H. Zhu, J. Yun, W. Zhao, Z. Zhang, Y. Wang, Shape-controlled SnO and their improved properties in the field of gas sensor, photocatalysis, and lithium-ion battery, Sens Actuators B Chem. 372 (2022) 132622. https://doi.org/10.1016/j.snb.2022.132622.

[102] Z. Guo, X. Han, Z. Zhang, X. Zhang, M. Liang, D. Wu, W. Yuan, High active crystalline {1 1 0} facets with high surface energy in Tin monoxide photocatalyst, Inorg Chem Commun. 134 (2021) 109043. https://doi.org/10.1016/J.INOCHE.2021.109043.

[103] G. Kresse, J. Furthmüller, Efficient iterative schemes for ab initio total-energy calculations using a plane-wave basis set, Phys Rev B Condens Matter Mater Phys. 54 (1996) 11169–11186. https://doi.org/10.1103/PhysRevB.54.11169.

[104] P.E. Blöchl, Projector augmented-wave method, Phys Rev B. 50 (1994) 17953–17979. https://doi.org/10.1103/PhysRevB.50.17953.

[105] J.P. Perdew, K. Burke, M. Ernzerhof, Generalized gradient approximation made simple, Phys Rev Lett. 77 (1996) 3865–3868. https://doi.org/10.1103/PhysRevLett.77.3865.

[106] M.G. Stanford, K. Yang, Y. Chyan, C. Kittrell, J.M. Tour, Laser-Induced Graphene for Flexible and Embeddable Gas Sensors, ACS Nano. 13 (2019) 3474–3482. https://doi.org/10.1021/acsnano.8b09622.

[107] G. Paterakis, E. Vaughan, D.R. Gawade, R. Murray, G. Gorgolis, S. Matsalis, G. Anagnostopoulos, J.L. Buckley, B. O'Flynn, A.J. Quinn, D. Iacopino, C. Galiotis, Highly Sensitive and Ultra-Responsive Humidity Sensors Based on Graphene Oxide Active Layers and High Surface Area Laser-Induced Graphene Electrodes, Nanomaterials. 12 (2022). https://doi.org/10.3390/nano12152684.

[108] K.J. Saji, K. Tian, M. Snure, A. Tiwari, K.J. Saji, K. Tian, A. Tiwari, M. Snure, 2D Tin Monoxide—An Unexplored p-Type van der Waals Semiconductor: Material Characteristics and Field Effect Transistors, Adv Electron Mater. 2 (2016) 1500453. https://doi.org/10.1002/AELM.201500453.

[109] A. Vázquez-López, D. Maestre, J. Ramírez-Castellanos, A. Cremades, In situ local oxidation of sno induced by laser irradiation: A stability study, Nanomaterials. 11 (2021). https://doi.org/10.3390/nano11040976.

[110] K.J. Saji, Y.P. Venkata Subbaiah, K. Tian, A. Tiwari, P-type SnO thin films and SnO/ZnO heterostructures for all-oxide electronic and optoelectronic device applications, Thin Solid Films. 605 (2016) 193–201. https://doi.org/10.1016/J.TSF.2015.09.026.

[111] Z. Ouyang, W. Wang, M. Dai, B. Zhang, J. Gong, M. Li, L. Qin, H. Sun, Research Progress of p-Type Oxide Thin-Film Transistors, Materials 2022, Vol. 15, Page 4781. 15 (2022) 4781. https://doi.org/10.3390/MA15144781.

[112] K.J. Saji, A.P.R. Mary, Tin Oxide Based P and N-Type Thin Film Transistors Developed by RF Sputtering, ECS Journal of Solid State Science and Technology. 4 (2015) Q101–Q104. https://doi.org/10.1149/2.0091509JSS/XML.

[113] M. Hübner, D. Koziej, J.D. Grunwaldt, U. Weimar, N. Barsan, An Au clusters related spill-over sensitization mechanism in SnO2-based gas sensors identified by operando HERFD-XAS, work function changes, DC resistance and catalytic conversion studies, Physical Chemistry Chemical Physics. 14 (2012) 13249–13254. https://doi.org/10.1039/C2CP41349C.

[114] H. Yu, S. Gao, X. Cheng, P. Wang, X. Zhang, Y. Xu, H. Zhao, L. Huo, Morphology controllable Fe2O3 nanostructures derived from Fe-based metal-organic frameworks for enhanced humidity sensing performances, Sens Actuators B Chem. 297 (2019) 126744. https://doi.org/10.1016/j.snb.2019.126744.

[115] G. Henkelman, A. Arnaldsson, H. Jónsson, A fast and robust algorithm for Bader decomposition of charge density, Comput Mater Sci. 36 (2006) 354–360. https://doi.org/10.1016/J.COMMATSCI.2005.04.010.

[116] K.J. Saji, Y.P. Venkata Subbaiah, K. Tian, A. Tiwari, P-type SnO thin films and SnO/ZnO heterostructures for all-oxide electronic and optoelectronic device applications, Thin Solid Films. 605 (2016) 193–201. https://doi.org/10.1016/J.TSF.2015.09.026.

[117] N.X. Thai, M. Tonezzer, L. Masera, H. Nguyen, N. van Duy, N.D. Hoa, Multi gas sensors using one nanomaterial, temperature gradient, and machine learning algorithms for discrimination of gases and their concentration, Anal Chim Acta. 1124 (2020) 85–93. https://doi.org/10.1016/j.aca.2020.05.015.

[118] T. Itoh, Y. Koyama, W. Shin, T. Akamatsu, A. Tsuruta, Y. Masuda, K. Uchiyama, Selective detection of target volatile organic compounds in contaminated air using sensor array with machine learning: Aging notes and mold smells in simulated automobile interior contaminant gases, Sensors (Switzerland). 20 (2020). https://doi.org/10.3390/s20092687.

[119] Z. Zhu, C.T. Kao, R.J. Wu, A highly sensitive ethanol sensor based on Ag@TiO2 nanoparticles at room temperature, Appl Surf Sci. 320 (2014) 348–355. https://doi.org/10.1016/J.APSUSC.2014.09.108.

[120] S.M. Majhi, A. Mirzaei, H.W. Kim, S.S. Kim, T.W. Kim, Recent advances in energy-saving chemiresistive gas sensors: A review, Nano Energy. 79 (2021). https://doi.org/10.1016/J.NANOEN.2020.105369.